Advances in Geo-Energy Research

Vol. 13, No. 2, p. 106-118, 2024

Original article

Simulation of CO_2 enhanced oil recovery and storage in shale oil reservoirs: Unveiling the impacts of nano-confinement and oil composition

Yilei Song[1,2], Zhaojie Song[2,3]*, Zhangxin Chen[4,5], Yasi Mo[1], Qiancheng Zhou[2,3], Shouceng Tian[1,2]*

[1]*School of Petroleum, China University of Petroleum-Beijing at Karamay, Karamay 834000, P. R. China*

[2]*National Key Laboratory of Petroleum Resources and Engineering, China University of Petroleum (Beijing), Beijing 102249, P. R. China*

[3]*Unconventional Petroleum Research Institute, China University of Petroleum (Beijing), Beijing 102249, P. R. China*

[4]*Eastern Institute of Technology, Ningbo 315200, P. R. China*

[5]*Department of Chemical and Petroleum Engineering, University of Calgary, Calgary T2N1N4, Canada*

Keywords:
Shale oil reservoirs
CO_2 enhanced oil recovery
CO_2 storage
nano-confinement

Cited as:
Song, Y., Song, Z., Chen, Z., Mo, Y., Zhou, Q., Tian, S. Simulation of CO_2 enhanced oil recovery and storage in shale oil reservoirs: Unveiling the impacts of nano-confinement and oil composition. Advances in Geo-Energy Research, 2024, 13(2): 106-118.
https://doi.org/10.46690/ager.2024.08.05

Abstract:
CO_2 injection into oil reservoirs is expected to achieve enhanced oil recovery along with the benefit of carbon storage, while the application potential of this strategy for shale reservoirs is unclear. In this work, a numerical model for multiphase flow in shale oil reservoirs is developed to investigate the impacts of nano-confinement and oil composition on shale oil recovery and CO_2 storage efficiency. Two shale oils with different maturity levels are selected, with the higher-maturity shale oil containing lighter components. The results indicate that the saturation pressure of the lower-maturity shale oil continues to increase with increasing CO_2 injection, while that of the higher-maturity shale oil continues to decrease. The recovery factor and CO_2 storage rate for higher-maturity shale oil after CO_2 huff-n-puff are 12.02% and 44.76%, respectively, while for lower-maturity shale oil, these are 4.41% and 69.33%, respectively. These data confirm the potential of enhanced oil recovery in conjunction with carbon storage in shale oil reservoirs. Under the nano-confinement impact, a decrease in the oil saturation in the matrix during production is reduced, which leads to a significant increase in oil production and a significant decrease in gas production. The oil production of the two kinds of shale oil is comparable, but the gas production of higher-maturity shale oil is significantly higher. Nano-confinement shows a greater impact on the bubble point pressure of higher-maturity shale oil and a more pronounced impact on the production of lower-maturity shale oil.

1. Introduction

The geological storage of CO_2 is an important alternative of carbon storage (Chen et al., 2022; Kivi et al., 2022). However, standalone CO_2 geological storage projects are costly and not suitable for large-scale promotion (Tyne et al., 2021). Carbon Capture, Utilization, and Storage with Enhanced Oil Recovery could simultaneously achieve storage of CO_2 and improve oil recovery, thereby saving carbon storage costs (Orr Jr and Taber, 1984). On the other hand, shale oil resources are abundant with enormous development potential, whereas their development is extremely challenging (Jin et al., 2022; Yang et al., 2024). It has been demonstrated that CO_2 can effectively improve shale oil recovery (Song et al., 2024a). However, the factors affecting the simultaneous realization of carbon storage and enhanced shale oil recovery as well as the potential of this strategy are not yet clear.

Shale oil reservoirs are widely distributed in nanoscale pore-throat systems with strong solid-fluid interaction forces (Cai et al., 2018; Liu et al., 2022a; Chu and Zhang, 2023). This leads to a significant nano-confinement impact on fluids

Yandy Scientific Press

*Corresponding author.
E-mail address: syl@cupk.edu.cn (Y. Song); songz@cup.edu.cn (Z. Song); zhachen@ucalgary.ca (Z. Chen); moyasi@cupk.edu.cn (Y. Mo); 2022216663@student.cup.edu.cn (Q. Zhou); tscsydx@163.com (S. Tian).

Received May 7, 2024; revised June 1, 2024; accepted June 25, 2024; available online June 30, 2024.

(Li et al., 2024), which is characterized by a high adsorption ratio and critical property shifts in pure components (Wang et al., 2021; Meng et al., 2024). The properties of fluids and interphase mass transfer exhibit intricate variations under the impact of nano-confinement, resulting in complex phase behavior and flow characteristics in shale oil-CO_2 systems (Song et al., 2024b; Yuan et al., 2024). Further exploration is imperative to fully comprehend the phase and flow characteristics throughout the CO_2 injection process in shale oil reservoirs, and to provide vital guidance for CO_2 enhanced oil recovery and storage programs.

Researchers have conducted numerous experiments and simulations to investigate the phase behavior and flow mechanisms in shale oil-CO_2 systems (Wang et al., 2023b; Zhou et al., 2023). In terms of phase behavior, the existing research methods mainly include experimental methods (Luo et al., 2019), molecular simulation methods (Huang et al., 2024), and equation of state (EOS) methods (Xiong et al., 2021). A widely accepted approach is to build phase behavior calculation models considering the nano-confinement impacts by calibrating an EOS based on benchmark values provided by experimental methods and molecular simulations. It has been shown that nano-confinement impacts reduce the interfacial tension between the vapor and liquid phases, which in turn makes CO_2 and oil more miscible (Zhang et al., 2022a). In micro-scale flow research, the main methods include in-house experiments (Elturki and Imqam, 2023), molecular dynamics simulations (Liu et al., 2022b), lattice Boltzmann simulations (Zhang and Sun, 2019), and pore network modeling (Zhang et al., 2022b). Due to the influence of solid-fluid interactions, the flow characteristics of fluids inside nanoscale pores are not only affected by the properties of the fluids but also constrained by pore size (Shan et al., 2022; Cheng et al., 2023). In macro-scale flow studies, the main focus is on modeling multiphase fluid flow in shale reservoirs by the modification of traditional numerical simulators (Lee and Lee, 2019; Shabib-Asl et al., 2020). The development of multiphase flow numerical simulation methods suitable for multiscale media in shale oil reservoirs is an essential requirement for elucidating the phase behavior and flow production mechanisms in oil-CO_2 systems in these reservoirs.

Recently, scholars have been dedicated to constructing macro-scale numerical models for the study of dynamic production in shale reservoirs (Tang et al., 2023; Wang et al., 2023c). Sun et al. (2013) developed a numerical simulation method for CO_2 injection into shale gas reservoirs to enhance recovery while considering coupled transport mechanisms such as viscous flow, Knudsen's diffusion and molecular diffusion. Jiang and Younis (2016) established a compositional model suitable for shale gas reservoirs, taking into account transport mechanisms such as multi-component apparent permeability, adsorption and molecular diffusion. Zhang et al. (2017) developed a phase equilibrium calculation method and a numerical simulation method that account for capillary force in nanoscale pores. They investigated the impact of capillary pressure on oil and gas production in the Bakken shale reservoir. Li et al. (2019) conducted laboratory experiments to construct a micro-scale numerical model for CO_2 injection in shale oil recovery, which considers the molecular diffusion mechanism in nanoscale spaces. They analyzed the influence of different injection parameters on shale oil recovery. Despite these advances, the existing studies often directly incorporate critical property shift parameters into numerical models without modifying their EOS (Wan and Mu, 2018). Consequently, the impact of nano-confinement on the flow production characteristics and storage effectiveness of CO_2 injection in shale oil reservoirs is still unknown. Furthermore, previous studies often focus on a specific shale oil, while the differences in phase behavior and flow characteristics after CO_2 injection into shale oils with different compositions remain unexplored.

As a result of hydraulic fracturing in shale reservoirs, a complex network of fractures is formed (Wang et al., 2023a; He et al., 2024; Murugesu et al., 2024). Typically, scholars use locally refined grids to simulate artificial fractures; however, this method is challenging when simulating inclined fractures and has limitations regarding the number of artificial fractures (Jiang and Younis, 2017). To address this issue, some researchers have employed discrete fracture models to simulate artificial fractures (Liu et al., 2024). Shakiba et al. (2018) established a numerical model for unconventional oil and gas reservoirs based on an embedded discrete fracture model (EDFM). Bai et al., 2021 developed a compositional model based on EDFM to investigate the impact of hydraulic fractures and natural fractures on shale oil development. Ţene et al., 2017 proposed a projection-based embedded discrete fracture model (pEDFM), reducing errors in handling low-conductivity fractures with EDFM. From the literature, it is evident that discrete fracture models have been widely applied in the numerical simulation of fractured reservoirs (Jia et al., 2023; Hui et al., 2023); however, the existing research mainly focuses on oil-water two-phase flow and the hydraulic fracturing stage.

In this study, a numerical model for multiphase flow in shale oil reservoirs is developed using pEDFM and a phase behavior module considering nano-confinement impacts. Two shale oils with different maturity levels are selected, with the higher-maturity shale oil containing lighter components such as C_1. Using this numerical model, the impacts of nano-confinement and shale oil composition on the recovery factor and CO_2 storage efficiency are clarified by analyzing the production dynamics data (e.g., oil saturation distribution, pressure distribution, and CO_2 distribution) in shale reservoirs after CO_2 huff-n-puff.

2. Multiphase flow numerical model

In the numerical model proposed in this study, the following assumptions are made:

1) The multi-scale properties and inhomogeneity of the reservoir are considered, ignoring the compressibility of the rock;
2) The vapor and liquid phases attain immediate equilibrium upon contact, with nano-confinement impacts incorporated into phase equilibrium calculations;
3) The flow process remains isothermal.

All relevant operations are implemented using MATLAB programming.

2.1 Governing equations

The mass conservation equations for the vapor or liquid phases are presented as (Deng et al., 2023):

$$\partial_t\left[\phi\left(\rho_L S_L X_i+\rho_V S_V Y_i\right)\right]+\nabla\cdot\left(\rho_L X_i\vec{v_L}+\rho_V Y_i\vec{v_v}\right)-\frac{\rho_L X_i q_L+\rho_V Y_i q_V}{V}=0 \tag{1}$$

The mass conservation equation for the water phase is as follows:

$$\partial_t\left(\phi\rho_W S_W\right)+\nabla\cdot\left(\rho_W\vec{v_W}\right)-\frac{\rho_W q_W}{V}=0 \tag{2}$$

where ϕ represents porosity; ρ_L, ρ_V and ρ_W are the densities of the liquid (oil) phase, vapor phase and water phase, respectively; S_L, S_V and S_W represent the saturations of the liquid phase, vapor phase and water phase, respectively; X_i and Y_i denote the mass fractions of component i in the liquid and vapor phases, respectively; $\vec{v_L}$, $\vec{v_V}$ and $\vec{v_W}$ are the velocities of the liquid phase, vapor phase and water phase, respectively; q_L, q_V and q_W are the source/sink terms for the liquid phase, vapor phase and water phase, respectively; V stands for volume. The flow velocity is calculated using Darcy's law:

$$\vec{v}=-K\frac{K_r}{\mu}\left(\nabla P-\rho g\nabla z\right) \tag{3}$$

where K and K_r represent absolute and relative permeability, respectively; P is the fluid pressure; z denotes the relative vertical positing; g stands for the gravitational acceleration.

The saturation constraint equation and component constraint relationships are as follows:

$$\begin{cases} S_W+S_L+S_V=1 \\ \sum_{i=1}^{N}x_i=\sum_{i=1}^{N}y_i=\sum_{i=1}^{N}z_i=1 \end{cases} \tag{4}$$

where x_i, y_i, z_i represent the mole fraction of component i in the liquid phase, vapor phase and overall mixture, respectively.

2.2 Phase behavior module

In this work, the A-PR-EOS proposed by Song et al. (2020) is employed to describe the fluid phase behavior, such as:

$$P=\frac{RT}{\frac{V_m}{1-\gamma\beta}-b}-\frac{a}{\frac{V_m}{1-\gamma\beta}\left(\frac{V_m}{1-\gamma\beta}+b\right)+b\left(\frac{V_m}{1-\gamma\beta}-b\right)} \tag{5}$$

where R, T and V_m represent universal gas constant, temperature, and mole volume, respectively; a and b are the attractive and repulsive parameters, respectively; γ and β represent dimensionless adsorption radius and reduced adsorption density, respectively.

The A-PR-EOS can take into account the effect of fluid adsorption on the phase behavior. The EOS is related to pore size, since the adsorption parameters γ and β vary with pore size. It is verified that A-PR-EOS can be used to predict the fluid phase behavior in pores with a pore radius larger than 2 nm (Song et al., 2020). The criterion for fluid phase equilibrium is that the fugacity (f) of each component is equal between the vapor phase and the liquid phase. The formula for calculating the fugacity based on A-PR-EOS and van der Waals mixing rules is presented as:

$$\begin{aligned}
\ln\frac{f_{iL}}{x_i P}&=-\ln(Z_L-B_L)+\frac{b_i}{b}(Z_L-1)+\frac{A_L}{2\sqrt{2}B_L}\cdot\left[\frac{2}{a}\sqrt{a_i}\sum_{j=1}^{N_c}z_j\sqrt{a_j}(1-\delta_{ij})-\frac{b_i}{b}\right]\cdot\ln\frac{Z_L+B_L(1+\sqrt{2})}{Z_L+B_L(1-\sqrt{2})}\\
\ln\frac{f_{iV}}{y_i P}&=-\ln(Z_V-B_V)+\frac{b_i}{b}(Z_V-1)+\frac{A_V}{2\sqrt{2}B_V}\cdot\left[\frac{2}{a}\sqrt{a_i}\sum_{j=1}^{N_c}z_j\sqrt{a_j}(1-\delta_{ij})-\frac{b_i}{b}\right]\cdot\ln\frac{Z_V+B_V(1+\sqrt{2})}{Z_V+B_V(1-\sqrt{2})}\\
A_L&=\frac{aP}{(RT)^2}\\
B_L&=\frac{bp}{RT}(1-\gamma\beta)\\
A_V&=\frac{aP}{(RT)^2}\\
B_V&=\frac{bP}{RT}(1-\gamma\beta)
\end{aligned} \tag{6}$$

where subscripts L and V represent the liquid phase and vapor phase, respectively; x, y and z are the mole fractions of the liquid phase, vapor phase, and overall mixture, respectively; Z, B, A and δ represent the compressibility factor, attractive parameters, repulsive parameters, and binary interaction coefficient, respectively

During the phase equilibrium calculation, the impact of the critical properties of pure components varying with pore size is taken into account. The formulas for calculating the critical pressure (P_{cn}) and critical temperature (T_{cn}) of the substance in nanopores derived from the A-PR-EOS are as follows (Song et al., 2020):

$$P_{cn}=p_c\left[1-1.3588\left(\frac{\sigma_{LJ}}{R_p}\right)^{0.7878}+0.1646\left(\frac{\sigma_{LJ}}{R_p}\right)^{1.3588}\right] \tag{7}$$

$$T_{cn}=T_c\left[1-0.6794\left(\frac{\sigma_{RJ}}{R_p}\right)^{0.7878}\right] \tag{8}$$

where P_c and T_c represent the critical pressure and critical temperature under the bulk phase, respectively; σ_{LJ} is the Lennard-Jones length parameter; R_p stands for pore radius.

2.3 Fracture module

To model the hydraulic fractures, this paper employs the pEDFM. The core concept behind pEDFM involves projecting the fracture located within fracture elements onto three out

Table 1. Fluid composition and physical parameters of shale oil #1.

Components	z_i (mol%)	M_W	T_c (K)	P_c (kPa)	ω	χ
N_2	0.17	28.01	126.20	3,394.39	0.040	41.0
CO_2	0.12	44.01	304.20	7,376.46	0.225	78.0
C_1	65.22	16.04	190.60	4,600.16	0.008	77.3
C_2	12.79	30.07	305.40	4,883.87	0.098	108.9
C_3	4.72	44.10	369.80	4,245.52	0.152	151.9
C_4	1.80	58.12	425.20	3,799.69	0.193	191.7
C_5	0.42	72.15	469.60	3,374.12	0.251	233.9
C_6	0.66	86.18	507.40	2,968.82	0.296	271.0
C_7-C_{13}	5.99	134.21	607.82	2,325.70	0.479	385.3
C_{14}-C_{18}	3.64	219.53	715.09	1,723.17	0.731	578.0
C_{19}-C_{23}	2.52	287.59	763.36	1,594.92	0.913	735.4
C_{24}-C_{38}	1.97	385.63	857.43	1,435.49	1.125	976.8

of the six neighboring elements of the matrix unit where the fracture is situated (Ţene et al., 2017). If the fracture is positioned at the interface between two matrix units, pEDFM transforms into a simplified version known as DFM. The formula for seepage flow is outlined as follows (Lie and Møyner, 2021):

$$\begin{cases} Q^{nnc} = T^{nnc}\left(p_f - p_m\right) \\ Q^{nnc} = -Q^{nnc} \\ T^{nnc} = \dfrac{K^{nnc}A^{nnc}}{d^{nnc}} \end{cases} \tag{9}$$

where Q^{nnc} represents the flux through non-adjacent connections; T^{nnc} denotes the conduction coefficient for non-adjacent connections; p_f and p_m are the pressures in the fracture and matrix, respectively; K^{nnc} denotes the permeability of non-adjacent link pairs; A^{nnc} is the contact area of non-adjacent link pairs; d^{nnc} stands for the distance from the matrix grid center to the fracture grid center. The above approach seamlessly incorporates fractures into the matrix grid system by augmenting Eq. (1) with the seepage flow expressed through source/sink terms. During the flow simulation process, the composition, density, viscosity, and other physical properties of the phases in both the matrix and fractures are calculated in real time using the multiphase behavior module considering nano-confinement.

3. Fluid and geological model description

3.1 Composition and physical properties of shale oils

In this study, two shale oils from a medium-high maturity continental shale reservoir in Northeast China are selected to investigate the production dynamics during CO_2 Enhanced Oil Recovery and storage. Vitrinite reflectance (R_o) is an important parameter for characterizing maturity. Shale oils with higher R_o are generally of higher maturity, and R_o values for medium-high maturity shale oils typically exceed 1.0%. Shale oil #1, possessing a higher maturity ($R_o = 1.45\%$) with a reservoir temperature of 374.72 K and a reservoir pressure of 35.50 MPa, and shale oil #2, with lower maturity ($R_o = 1.15\%$) characterized by a reservoir temperature of 377.25 K and a reservoir pressure of 37.05 MPa, are chosen. To analyze the shale oil compositions, single-stage degassing experiments are conducted under reservoir temperature and pressure conditions. In addition, constant composition expansion experiments are performed to test parameters such as relative volume and bubble point pressure (P_b). To enhance the accuracy of the phase calculation module, the experimental data are utilized for the delineation of the proposed components and the correction of physical parameters, including the critical temperature, critical pressure, acentric factor, and binary interaction parameters. The composition and physical parameters of shale oil #1 and #2 are presented in Tables 1 and 2, respectively. M_W, ω and χ are molecular weight, acentric factor and parachor, respectively. Of these, the composition data related to shale oil #2 are adapted from Song et al. (2024b). The results reveal that shale oil #1 boasts a high C_1 content of up to 65.22 mol%, while the C_7^+ content accounts for only 14.1 mol%. According to the ternary phase diagram method, this oil is classified as highly volatile oil. Meanwhile, shale oil #2 exhibits a C_1 content of 46.66 mol% and a C_7^+ content of 32.56 mol%, classifying it as light crude oil.

3.2 Description of the three-dimensional geological model

The effectiveness and mechanism of CO_2 injection for enhanced shale oil recovery and carbon storage are analyzed by observing the fluid mass transfer within the fracture-matrix system. To facilitate this process, a small three-dimensional (3D) geological model (30 m × 15 m × 0.5 m) is constructed based on the formation and fracturing construction parameters. A hydraulic fracture is established as an injection/production boundary (i.e., horizontal wells), measuring 11 m in length,

Table 2. Fluid composition and physical parameters of shale oil #2 (Song et al., 2024b).

Components	z_i (mol%)	M_W	T_c (K)	P_c (kPa)	ω	χ
N_2	0.27	28.01	126.20	3,394.39	0.040	41.0
CO_2	0.09	44.01	304.20	7,376.46	0.225	78.0
C_1	46.66	16.04	190.60	4,600.16	0.008	77.3
C_2	12.05	30.07	305.40	4,883.87	0.098	108.9
C_3	4.78	44.10	369.80	4,245.52	0.152	151.9
C_4	1.80	58.12	425.20	3,799.69	0.193	191.7
C_5	0.63	72.15	469.60	3,374.12	0.251	233.9
C_6	1.17	86.18	507.40	2,968.82	0.296	271.0
C_7-C_{13}	13.92	135.18	609.15	2,314.34	0.482	387.2
C_{14}-C_{18}	8.37	219.04	714.54	1,725.32	0.730	576.8
C_{19}-C_{23}	5.69	887.64	759.72	1,518.87	0.914	735.6
C_{24}-C_{38}	4.58	386.97	854.62	1,365.70	1.127	980.5

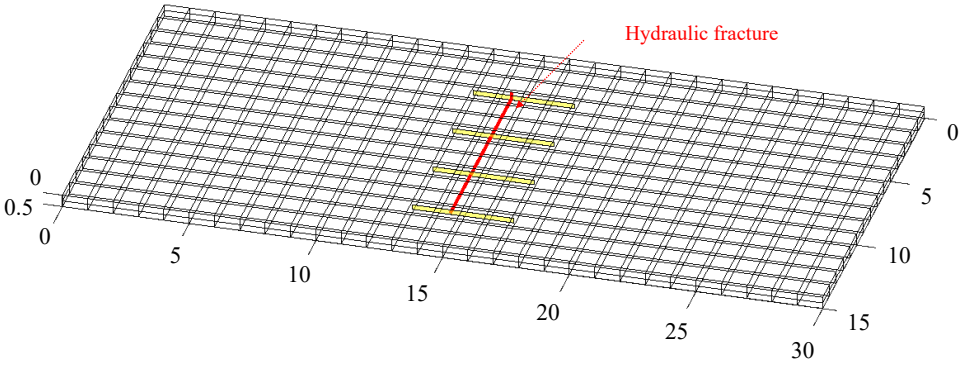

Fig. 1. 3D geological model for the fracture-matrix system.

as shown is Fig. 1. The matrix permeability is 0.0001×10^{-3} μm^2, and the matrix porosity ranges from 8% to 11%, with an average porosity of 9.8% (refer to Fig. 2). This fracture comprises four branches spaced 3 m apart, each with a length of 2 m, a height of 0.3 m, an aperture of 0.3 mm, a porosity of 25%, and a permeability of 0.1 μm^2. Using the numerical simulation approach and the three-dimensional geological model, the production behavior of shale oil reservoirs after CO_2 huff-n-puff is investigated. During the simulation, CO_2 is injected under a consistent injection pressure of 60 MPa (i.e., puff stage). After 6 months, injection is stopped for 15 days (i.e., soaking stage). Subsequently, the hydraulic fracture is opened and subjected to production under a constant pressure of 20 MPa for an additional 6 months (i.e., puff stage). Then, the impact of nano-confinement and oil composition on the dynamic production of shale oil are investigated.

4. Model performance validation

4.1 Ability to describe the phase behavior of fluids

The constant composition expansion processes of shale oil #1 and #2 are simulated using the phase behavior module. As can be seen from Fig. 3, the calculated results highly correspond with the experimental data. These data related to shale oil #2 are adapted from Song et al. (2024b). The saturation pressure of shale oil #1 is 38.75 MPa, exceeding the reservoir pressure, which indicates the coexistence of oil and vapor phases in the subsurface. Meanwhile, shale oil #2 shows a saturation pressure of 22.48 MPa, lower than the reservoir pressure, indicating that it exists as a pure oil phase in the subsurface. It can also be observed that, compared to shale oil #1, shale oil #2 exhibits a more pronounced inflection point in the constant composition expansion P-V relationship. Specifically, shale oil #2 shows a smaller change in relative volume when the pressure exceeds the saturation pressure, indicating poorer compressibility, and a larger change in relative volume change when the pressure is lower than the saturation pressure, indicating faster gas release. Furthermore,

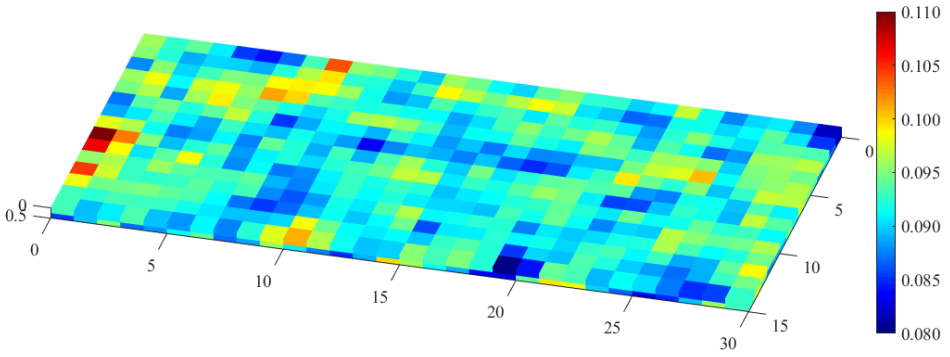

Fig. 2. 3D distribution of porosity in the shale matrix.

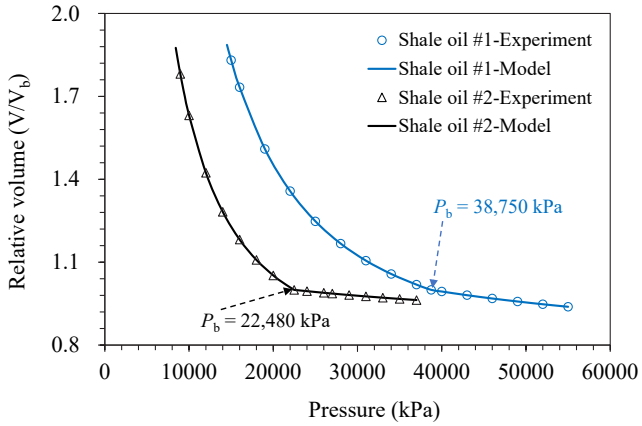

Fig. 3. Experimental and model-based P-V diagrams (Song et al., 2024b).

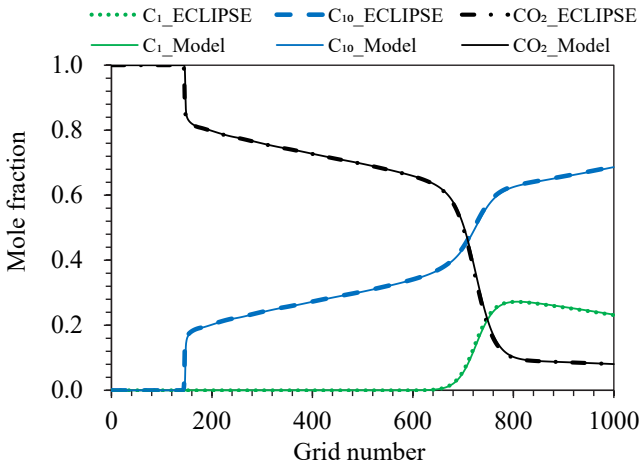

Fig. 4. Mole fraction from our model and ECLIPSE.

slim-tube experiments show that the minimum miscibility pressures of shale oil #1 and shale oil #2 with CO_2 are 20.00 and 27.50 MPa, respectively, demonstrating that both shale oils are miscible with CO_2 under reservoir conditions.

4.2 Ability to describe the flow process of fluids

In this section, flow within a conventional reservoir (with pore sizes greater than 100 nm, where nano-confinement can be neglected) is simulated using the model in this paper and commercial software. A one-dimensional reservoir comprising 1,000 grids is constructed and the CO_2 constant-pressure injection process is simulated using the multiphase flow numerical model and the ECLIPSE E300 software for comparison. The reservoir conditions are set to 423.15 K and 7.50 MPa, respectively, and the injection lasts for 1 year. As shown in Fig. 4, the fluid distribution results obtained through our numerical model and ECLIPSE are remarkably similar. This indicates that our numerical model offers a level of computational accuracy comparable to traditional numerical simulation software when simulating fluid flow processes in conventional reservoirs. Importantly, however, our model has the advantage of taking into account the impact of nano-confinement, therefore it is suitable for flow simulation research in shale reservoirs.

4.3 Ability to characterize nano-confinement

Phase behavior calculations are performed to determine the bubble point pressure of the CO_2-C_{10} binary system separately in bulk phase and under nanopore condition (R_p = 50 nm). The computed results are then compared with nanofluidic experimental data (Zhang et al., 2019). As shown in Table 3, the calculated results closely match the experimental data, indicating that our phase behavior module accurately describes nano-confinement impacts in nano-sized pores.

5. Results and discussion

5.1 P-T phase diagram of shale oil

The P-T phase diagram of shale oil provides significant support for understanding the phase stability regions, generation and storage conditions, as well as guiding reservoir development. In this study, the P-T phase diagrams of shale oils #1 and #2 at different pore sizes are calculated using the phase behavior module. As shown in Fig. 5, the phase diagram of shale oil #1 is notably positioned closer to the upper-left region due to the higher concentration of light components. The critical temperatures for the two shale oils are 514.08 and 652.97 K, respectively, with reservoir temperatures of 374.72 and 377.25 K, respectively. According to these data, the reservoir conditions for both shale oils are located to the left of the critical point and thus can be categorized as either volatile oil or heavy oil. Under reservoir temperature

Table 3. Experimental and calculated bubble point pressure data for CO_2-C_{10} mixtures (Zhang et al., 2019).

Condition	$T = 318.65$ K			$T = 333.65$ K		
	Experiment (KPa)	Calculation (KPa)	Relative error	Experiment (KPa)	Calculation (KPa)	Relative error
Bulk phase	5,853	5,796	-0.97%	7,371	7,433	0.84%
Nanopore	5,355	5,295	-1.12%	6,930	7,001	1.0%

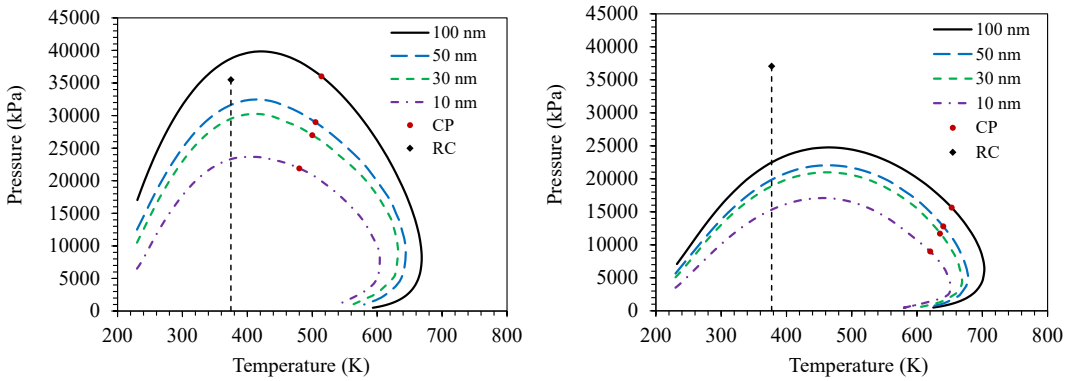

Fig. 5. P-T phase diagram of shale oils under the nano-confinement impact: (a) Shale oil #1 and (b) Shale oil #2. CP represents critical point and RC stands for reservoir condition.

conditions, the saturation pressure of shale oil #1 exceeds the reservoir pressure, resulting in a two-phase coexistence of oil and vapor underground. On the other hand, shale oil #2 exhibits a saturation pressure lower than the reservoir pressure, making it exist as a pure oil phase underground, consistent with the results of constant composition expansion experiments.

In accordance with Fig. 5, under the nano-confinement impact, the phase diagram of shale oils demonstrates a gradual contraction trend. The bubble point pressure, upper dew point pressure, critical pressure, and critical temperature of shale oils all significantly decrease as the pore size decreases. In particular, when the pore radius is less than 70 nm, shale oil #1 transitions from a coexistence of oil and vapor phases to a pure oil phase state. Furthermore, shale oil #1 experiences a more substantial reduction in bubble point pressure compared to shale oil #2. This is due to the nano-confinement impact suppressing the generation of vapor phase. Shale oil #1 contains a higher proportion of lighter components, resulting in a more pronounced drop in bubble point pressure.

5.2 Saturation pressure of shale oil after CO_2 injection

Here, the impact of CO_2 dissolution on the saturation pressure of shale oils is explored using the phase behavior module. As illustrated in Fig. 6, the saturation pressure of shale oil #1 consistently decreases with the increasing quantity of injected CO_2, while that of shale oil #2 consistently increases. This phenomenon is attributed to the minimal difference between the contents of C_1 and C_7^+ in shale oil #2, indicating the characteristic feature of the C_1-C_7^+ binary system on the phase diagram. The difference in the contents of C_1 and C_7^+ in shale oil #1 is obvious, so the phase diagram shows the characteristics of a C_1 single-component system. In a mixture, the saturation or bubble point pressures tend to approach the vapor pressures of the component with a higher content. Consequently, with an increase in CO_2 mole fraction, the saturation pressures of shale oil #2 gradually shift upward and to the left. For shale oil #1, the system undergoes transition from a C_1 single-component system to a C_1-CO_2 binary system as the CO_2 mole fraction increases, becoming a CO_2 single-component system at sufficiently high CO_2 content. Consequently, the phase diagram of shale oil #1 continues to contract with the increasing amount of injected CO_2, and the saturation pressure consistently decreases.

As seen in Fig. 6, the bubble point pressure of shale oil-CO_2 systems significantly decreases when nano-confinement is considered. Furthermore, the reduction in bubble point pressure is more pronounced with smaller pore sizes. Specifically, the bubble point pressure of shale oil #1 in the bulk phase decreases by 3.65 MPa when the CO_2 mole fraction increases to 20%, while in a 10 nm pore, it decreases by 0.40 MPa. Conversely, the bubble point pressure of shale oil #2 in the bulk phase increases by 1.89 MPa, whereas in a 10 nm pore, it increases by 1.40 MPa. From these data, it is evident that the influence of CO_2 mole fraction on the bubble point pressure of shale oil gradually diminishes with decreasing pore size, making the pore size emerge as a more critical factor affecting shale oil saturation pressure compared to the amount of injected CO_2.

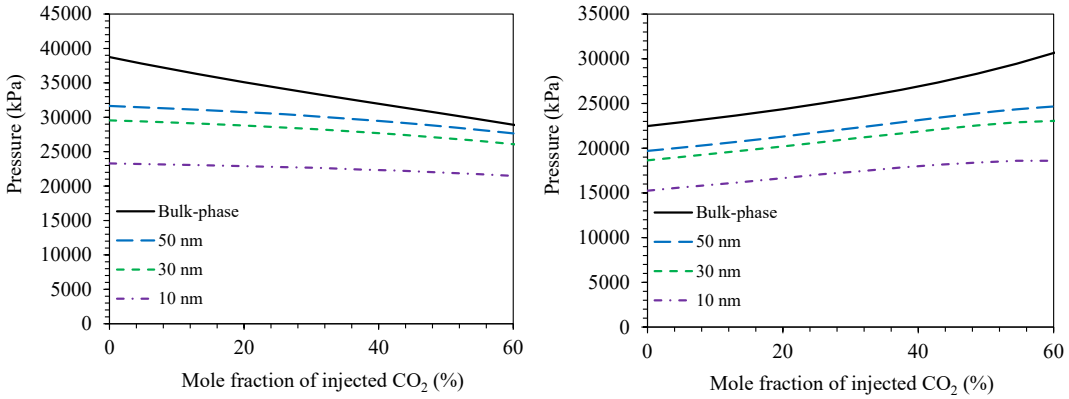

Fig. 6. Bubble point pressure of shale oils with CO_2 injection under the nano-confinement impact: (a) Shale oil #1 and (b) shale oil #2.

5.3 Cumulative oil and gas production after CO_2 huff-n-puff

Next, the recovery factor and CO_2 storage efficiency after CO_2 huff-n-puff are clarified using the numerical model. The results in Fig. 7 show that the volume of oil produced within the matrix significantly increases under the nano-confinement impact, while the gas volume decreases markedly. This is because the nano-confinement impact reduces the bubble point pressure of shale oil and promotes the dissolution of gas molecules in the oil phase, thereby inhibiting gas generation and increasing the flowability of the oil phase. Shale oil #1 exhibits a significantly higher produced gas-oil ratio when compared to shale oil #2. Specifically, the cumulative oil and gas production of shale oil #2 is 0.44 and 0.32 m^3, respectively, after half a year of production, while shale oil #1 produces 0.43 m^3 of oil cumulatively but has a high gas production of 2.22 m^3. Taking the nano-confinement impact into account, the cumulative oil production of shale oil #1 and #2 increases by 9.36% and 11.1%, respectively, while the cumulative gas production of shale oil #1 and #2 decreases by 5.97% and 11.82%, respectively. Therefore, nano-confinement has a greater impact on the oil and gas production of shale oil #2, which has a higher content of heavy components.

5.4 Oil saturation and pressure distribution after CO_2 huff-n-puff

Here, the distribution maps of oil saturation in the matrix are plotted to further analyze the production dynamic differences (see Fig. 8). The initial oil saturations in each grid within the matrix of shale oil #1 and #2 are both 100%. After continuous production for half a year, oil saturation significantly decreases with a greater reduction observed in the matrix of shale oil #1. Additionally, it can be observed that the reduction in oil saturation within the matrix of shale oil #2 decreases significantly under the impact of nano-confinement, while nano-confinement has little effect on oil saturation within the matrix of shale oil #1.

Nano-confinement exerts a more significant impact on oil saturation and oil production in shale oil #2 compared to shale oil #1. However, as demonstrated in Section 5.1, the decrease in bubble point pressure is greater for shale oil #1 for the same size of nanopores. This is primarily because shale oil #1 contains a higher proportion of light components, resulting in lower density and viscosity. As a result, it exhibits greater fluidity, which causes a faster pressure drop. According to Fig. 9, the pressure within the matrix of shale oil #1 is significantly lower compared to that in shale oil #2 after half a year of production. Therefore, despite the larger decrease in bubble point pressure for shale oil #1, its production dynamics are less affected by nano-confinement.

5.5 Stored CO_2 after CO_2 huff-n-puff

Fig. 10 illustrates the distribution of CO_2 mole fractions in the matrix of shale oils #1 and #2 after CO_2 injection (i.e., at the end of the puff stage). The results with nano-confinement show that a total of 1,171.05 mol of CO_2 is injected in the matrix of shale oil #1 and 276 grids have elevated CO_2 mole fractions (with a sweep coefficient of 29.61%), while a total of 401.66 mol of CO_2 is injected in the matrix of shale oil #2 and 159 grids have elevated CO_2 mole fractions (with a sweep coefficient of 17.06%). This means that a significantly greater amount of CO_2 penetrates into the matrix of shale oil #1 compared to shale oil #2 under the same injection pressure. This phenomenon is primarily attributed to shale oil #1 having greater fluidity, faster pressure propagation and more favorable interactions with CO_2. The results also indicate that nano-confinement has a relatively limited impact on the amount of stored CO_2 injection.

After six months of production considering nano-confinement, 606.92 mol of CO_2 is produced in the matrix of shale oil #1 and 123.19 mol of CO_2 is produced in the matrix of shale oil #2. At this time, the recovery factor and CO_2 storage rate in the matrix of shale oil #1 are 12.02% and 44.76%, respectively, while those in the matrix of shale oil #2 are 4.41% and 69.33%, respectively. The CO_2 storage rate is defined as the ratio of the number of moles of CO_2 trapped in the formation to the number of moles of CO_2

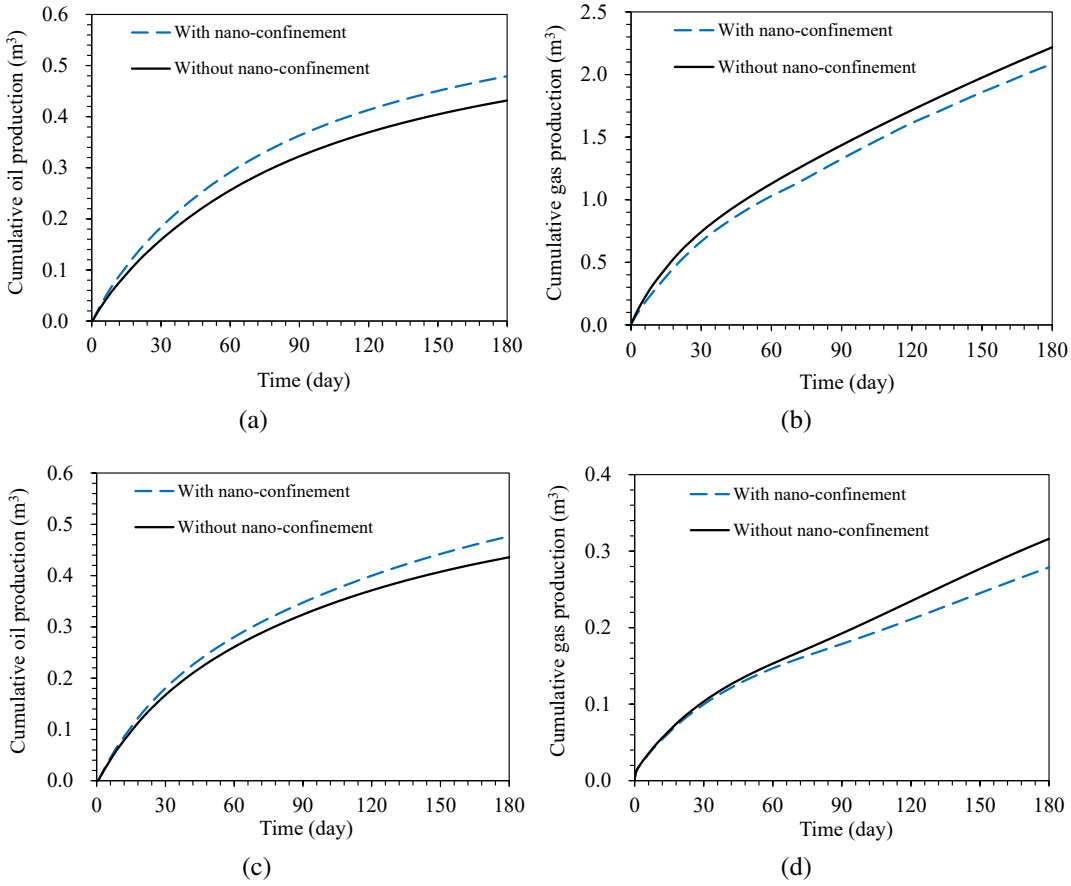

Fig. 7. Cumulative oil and gas production of shale oils: (a) Shale oil #1-cumulative oil, (b) shale oil #1-cumulative gas, (c) shale oil #2-cumulative oil and (d) shale oil #2-cumulative gas.

injected. This means that shale oils containing more heavy components yield lower shale oil recovery after CO_2 huff-n-puff and store less CO_2, but CO_2 escape is also more difficult. As can be seen in Fig. 11, the CO_2 content decreases significantly after production, but the number of grids of CO_2 mole fraction increase does not change significantly and even increases slightly. For example, the sweep coefficient of CO_2 in the matrix of shale oil #2 is slightly elevated from 17.06% to 17.27%. This indicates that some CO_2 is extracted out of the formation during production, but a considerable amount of CO_2 remains in the formation, which confirms the potential for carbon storage under increasing oil recovery factor.

6. Conclusions

In this study, a multiphase flow numerical model that considers the nano-confinement for shale oil reservoirs is developed and utilized to clarify the impacts of nano-confinement and shale oil composition on oil recovery and CO_2 storage efficiency. The key conclusions and findings are set out as follows:

1) Two shale oils with different maturity levels are selected for the study, with the higher-maturity shale oil containing more light components. The P-T phase diagram of shale oils exhibits a gradual contraction trend under the nano-confinement impact, and the bubble point pressure of the higher-maturity shale oil decreases more than that of the lower-maturity shale oil.
2) The bubble point pressure of the lower-maturity shale oil continues to decrease as the amount of CO_2 injection increases, while that of the higher-maturity shale oil continues to decrease. At pore radii of less than 50 nm, the bubble point pressure of shale oil is more affected by the pore size than the amount of CO_2 injected.
3) The higher-maturity shale oil shows a higher recovery factor after CO_2 huff-n-puff, but the low-maturity shale oil exhibits a higher CO_2 storage rate. The sweep area of CO_2 does not decrease significantly during the development process, which confirms the potential of carbon storage in conjunction with enhanced oil recovery in shale oil reservoirs.
4) The decrease in the oil saturation of the matrix is reduced under the nano-confinement impact, which leads to an increase in oil production and a decrease in gas production. Moreover, the impact of nano-confinement on the production of the lower-maturity shale oil is more pronounced.

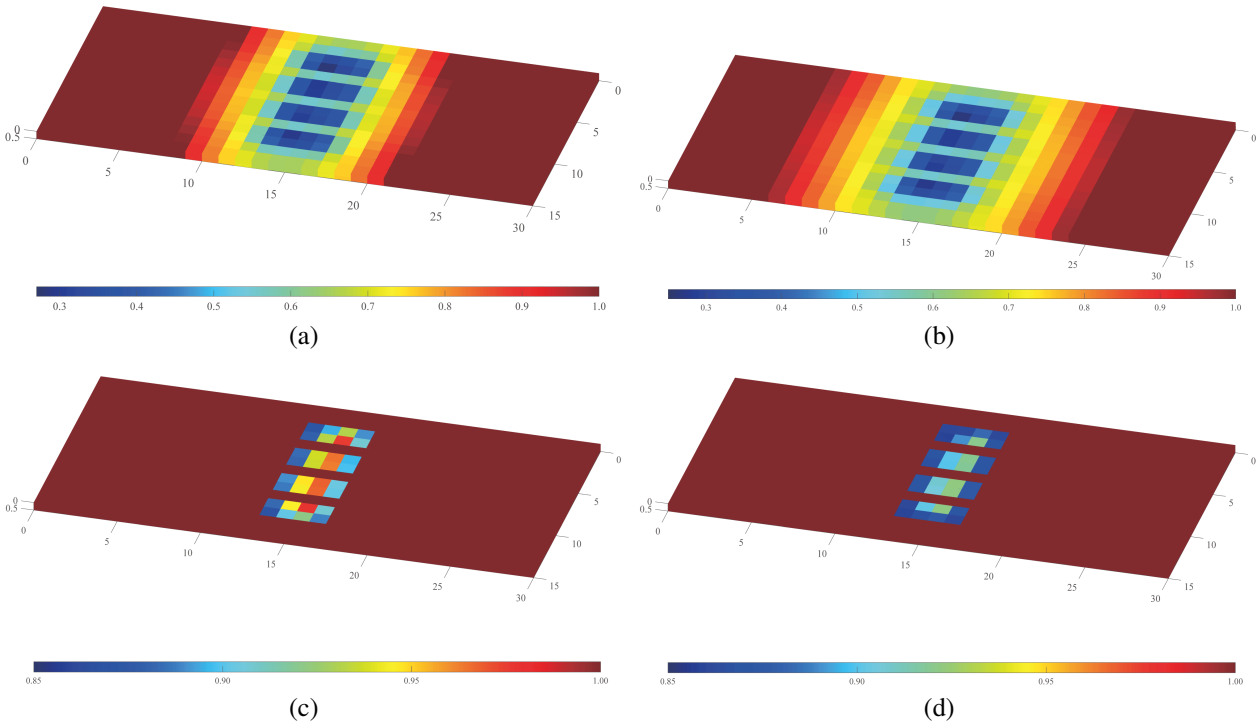

Fig. 8. Oil saturation distribution in the matrix of shale oils after half a year of production: (a) Shale oil #1-with nano-confinement, (b) shale oil #1-without nano-confinement, (c) shale oil #2-with nano-confinement and (d) shale oil #2-without nano-confinement.

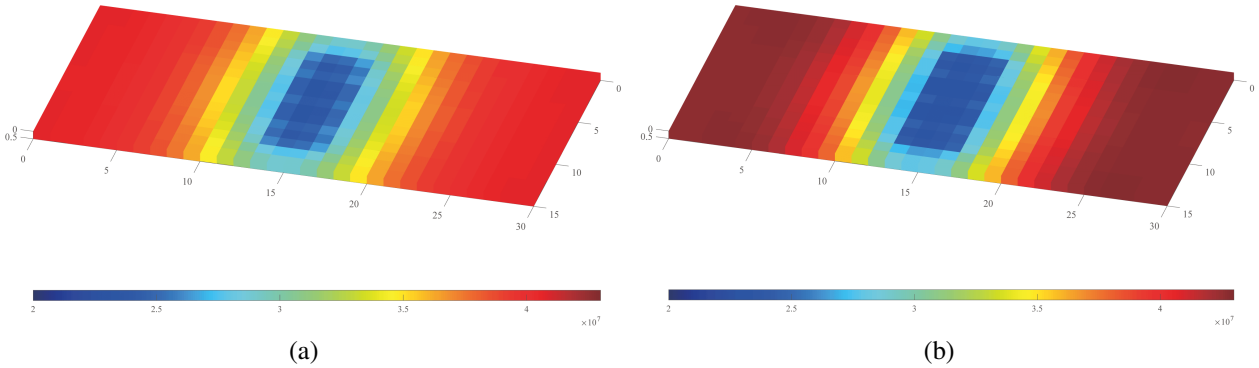

Fig. 9. Pressure distribution in the matrix of shale oils after production with nano-confinement: (a) Shale oil #1 and (b) shale oil #2.

Acknowledgements

The authors gratefully acknowledge the financial support of the National Natural Science Foundation of China (No. 52074319), the Heilongjiang Province Science and Technology Research Projects (No. DQYT-2022-JS-761) and the Science Foundation of China University of Petroleum-Beijing (No. 2462021QNXZ008).

Conflict of interest

The authors declare no competing interest.

References

Bai, Y., Liu, L., Fan, W., et al. Coupled compositional flow and geomechanics modeling of fractured shale oil reservoir with confined phase behavior. Journal of Petroleum Science and Engineering, 2021, 196: 107608.

Cai, J., Lin, D., Singh, H., et al. Shale gas transport model in 3D fractal porous media with variable pore sizes. Marine and Petroleum Geology, 2018, 98: 437-447.

Cheng, H., Wang, F., Guan, X., et al. A mathematical model for pre-Darcy flow in low permeability porous media with stress sensitivity and the boundary-layer effect.

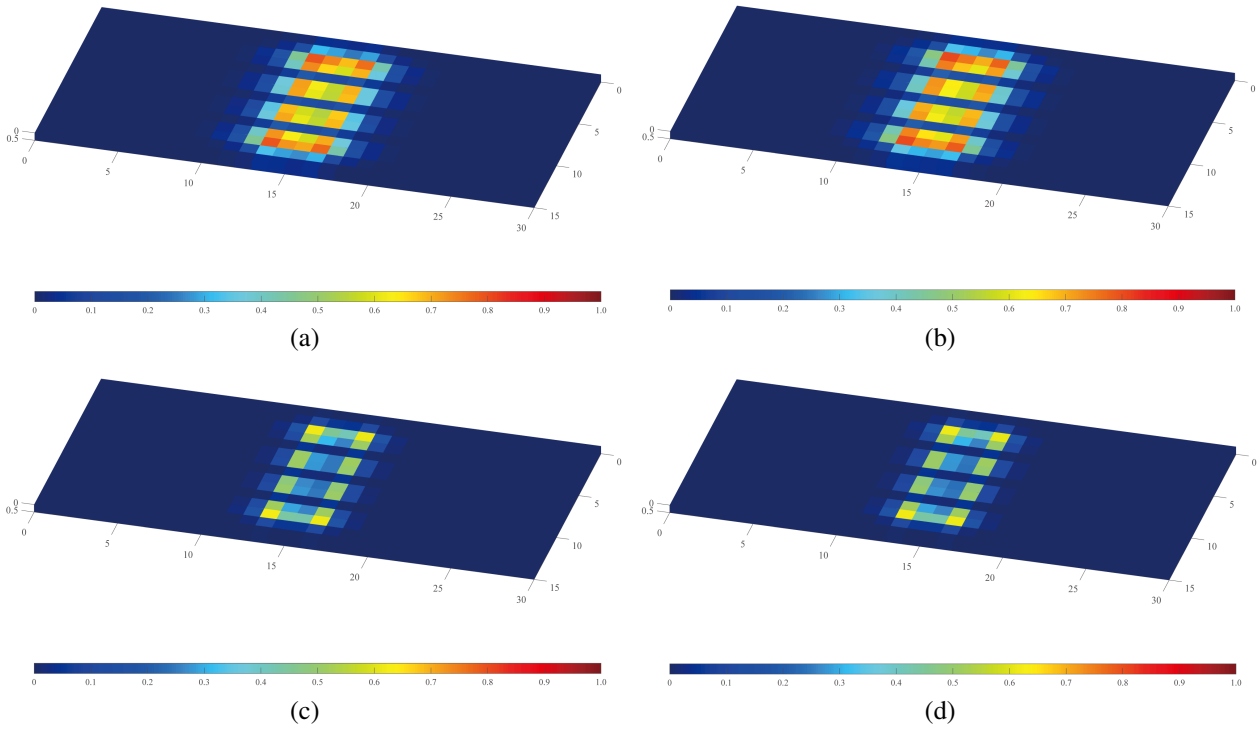

Fig. 10. CO_2 distribution in the matrix of shale oils after CO_2 injection: (a) Shale oil #1-with nano-confinement, (b) shale oil #1-without nano-confinement, (c) shale oil #2-with nano-confinement and (d) shale oil #2-without nano-confinement.

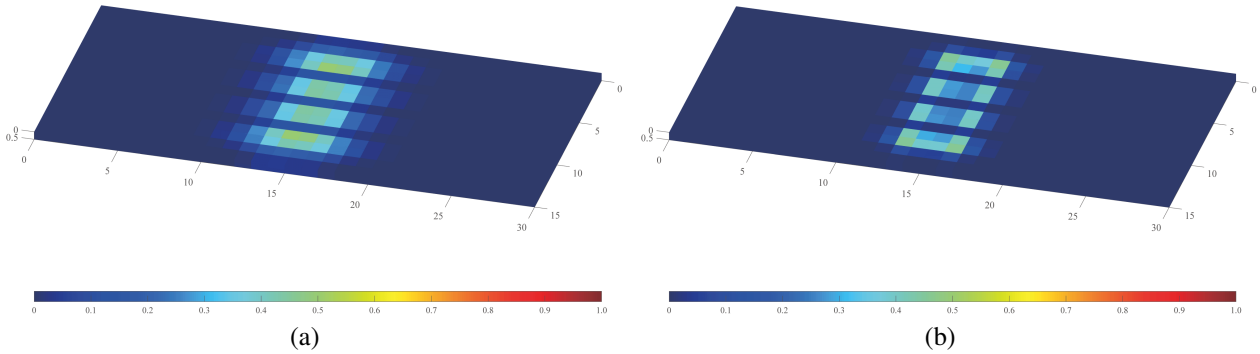

Fig. 11. CO_2 distribution in the matrix of shale oils after production with nano-confinement: (a) Shale oil #1 and (b) shale oil #2.

Engineering Geology, 2023, 324: 107257.

Chen, S., Liu, J., Zhang, Q., et al. A critical review on deployment planning and risk analysis of carbon capture, utilization, and storage (CCUS) toward carbon neutrality. Renewable and Sustainable Energy Reviews, 2022, 167: 112537.

Chu, W., Zhang, K. Fluid phase behavior of tight and shale reservoirs: Monte Carlo simulations. Advances in Geo-Energy Research, 2023, 7(2): 132-135.

Deng, P., Chen, Z., Peng, X., et al. Optimized lower pressure limit for condensate underground gas storage using a dynamic pseudo-component model. Energy, 2023, 285: 129505.

Elturki, M., Imqam, A. Experimental investigation of asphaltene deposition and its impact on oil recovery in Eagle Ford Shale during miscible and immiscible CO_2 huff-n-puff gas injection. Energy & Fuels, 2023, 37(4): 2993-3010.

He, Q., Wang, Z., Liu, C., et al. Identifying nonuniform distributions of rock properties and hydraulic fracture trajectories through deep learning in unconventional reservoirs. Energy, 2024, 291: 130329.

Huang, C., Tian, L., Wang, J., et al. Water-CO_2 wettability on sandstone surface with asphaltene adsorption: Molecular dynamics simulation. Fuel, 2024, 360: 130558.

Hui, G., Chen, Z., Schultz, R., et al. Intricate unconventional fracture networks provide fluid diffusion pathways to reactivate pre-existing faults in unconventional reservoirs.

Energy, 2023, 282: 128803.

Jiang, J., Younis, R. M. Compositional modeling of enhanced hydrocarbons recovery for fractured shale gas-condensate reservoirs with the effects of capillary pressure and multicomponent mechanisms. Journal of Natural Gas Science and Engineering, 2016, 34: 1262-1275.

Jiang, J., Younis, R. M. An improved projection-based embedded discrete fracture model (pEDFM) for multiphase flow in fractured reservoirs. Advances in Water Resources, 2017, 109, 267-289.

Jia, Z., Cheng, L., Feng, H., et al. Full composition numerical simulation of CO_2 utilization process in shale reservoir using projection-based embedded discrete fracture model (pEDFM) considering nano-confinement effect. Gas Science and Engineering, 2023, 111: 204932.

Jin, Z., Liang, X., Bai, Z. Exploration breakthrough and its significance of Gulong lacustrine shale oil in the Songliao Basin, Northeastern China. Energy Geoscience, 2022, 3(2): 120-125.

Kivi, I. R., Makhnenko, R. Y., Oldenburg, C. M., et al. Multilayered systems for permanent geologic storage of CO_2 at the gigatonne scale. Geophysical Research Letters, 2022, 49(24): e2022GL100443.

Lee, J. H., Lee, K. S. Investigation of asphaltene-derived formation damage and nano-confinement on the performance of CO_2 huff-n-puff in shale oil reservoirs. Journal of Petroleum Science and Engineering, 2019, 182: 106304.

Lie, K., Møyner, O. Advanced Modeling with the MATLAB Reservoir Simulation Toolbox. Cambridge, UK, Cambridge University Press, 2021.

Li, L., Su, Y., Sheng, J., et al. Experimental and numerical study on CO_2 sweep volume during CO_2 huff-n-puff enhanced oil recovery process in shale oil reservoirs. Energy & Fuels, 2019, 33(5): 4017-4032.

Li, M., Sun, M., Mohammadian, E., et al. Confinement effect in nanopores of shale and coal reservoirs: A review on experimental characterization methods. Gas Science and Engineering, 2024, 123: 205249.

Liu, B., Gao, S., Mohammadian, E., et al. Comprehensive outlook into critical roles of pressure, volume, and temperature (PVT) and phase behavior on the exploration and development of shale oil. Energy & Fuels, 2022a, 36(24): 14534-14553.

Liu, B., Liu, W., Pan, Z., et al. Supercritical CO_2 breaking through a water bridge and enhancing shale oil recovery: A molecular dynamics simulation study. Energy & Fuels, 2022b, 36(14): 7558-7568.

Liu, J., He, X., Huang, H., et al. Predicting gas flow rate in fractured shale reservoirs using discrete fracture model and GA-BP neural network method. Engineering Analysis with Boundary Elements, 2024, 159: 315-330.

Luo, S., Lutkenhaus, J. L., Nasrabadi, H. Experimental study of pore size distribution effect on phase transitions of hydrocarbons in nanoporous media. Fluid Phase Equilibria, 2019, 487: 8-15.

Meng, S., Liu, C., Liu, Y., et al. CO_2 utilization and sequestration in organic-rich shale from the nanoscale perspective. Applied Energy, 2024, 361: 122907.

Murugesu, M. P., Vega, B., Ross, C. M., et al. Coupled transport, reactivity, and mechanics in fractured shale caprocks. Water Resources Research, 2024, 60(1): e2023WR035482.

Orr Jr, F. M., Taber, J. J. Use of carbon dioxide in enhanced oil recovery. Science, 1984, 224(4649): 563-569.

Shabib-Asl, A., Plaksina, T., Moradi, B. Evaluation of nanopore confinement during CO_2 huff and puff process in liquid-rich shale formations. Computational Geosciences, 2020, 24(3): 1163-1178.

Shakiba, M., Cavalcante Filho, J. S. D. A., Sepehrnoori, K. Using embedded discrete fracture model (EDFM) in numerical simulation of complex hydraulic fracture networks calibrated by microseismic monitoring data. Journal of Natural Gas Science and Engineering, 2018, 55: 495-507.

Shan, B., Ju, L., Guo, Z., et al. Investigation of shale gas flows under confinement using a self-consistent multiscale approach. Advances in Geo-Energy Research, 2022, 6(6): 537-538.

Song, Y., Song, Z., Chen, Z., et al. Fluid phase behavior in multi-scale shale reservoirs with nano-confinement effect. Energy, 2024a, 289: 130027.

Song, Y., Song, Z., Meng, Y., et al. Multi-phase behavior and pore-scale flow in medium-high maturity continental shale reservoirs with Oil, CO_2, and water. Chemical Engineering Journal, 2024b, 484: 149679.

Song, Z., Song, Y., Guo, J., et al. Adsorption induced critical shifts of confined fluids in shale nanopores. Chemical Engineering Journal, 2020, 385: 123837.

Sun, H., Yao, J., Gao, S., et al. Numerical study of CO_2 enhanced natural gas recovery and sequestration in shale gas reservoirs. International Journal of Greenhouse Gas Control, 2013, 19: 406-419.

Tang, C., Zhou, W., Chen, Z., et al. Numerical simulation of CO_2 sequestration in shale gas reservoirs at reservoir scale coupled with enhanced gas recovery. Energy, 2023, 277: 127657.

Ţene, M., Bosma, S. B. M., Al Kobaisi, M. S., et al. Projection-based embedded discrete fracture model (pEDFM). Advances in Water Resources, 2017, 105: 205-216.

Tyne, R. L., Barry, P. H., Lawson, M., et al. Rapid microbial methanogenesis during CO_2 storage in hydrocarbon reservoirs. Nature, 2021, 600(7890): 670-674.

Wang, F., Xu, H., Liu, Y., et al. Mechanism of Low Chemical Agent Adsorption by High Pressure for Hydraulic Fracturing-Assisted Oil Displacement Technology: A Study of Molecular Dynamics Combined with Laboratory Experiments. Langmuir, 2023a, 39(46): 16628-16636.

Wang, H., Cai, J., Su, Y., et al. Pore-scale study on shale oil-CO_2-water miscibility, competitive adsorption, and multiphase flow behaviors. Langmuir, 2023b, 39(34): 12226-12234.

Wang, T., Tian, S., Li, G., et al. Molecular simulation of gas adsorption in shale nanopores: A critical review. Renewable and Sustainable Energy Reviews, 2021, 149:

111391.

Wang, Y., Dai, Z., Chen, L., et al. An integrated multi-scale model for CO_2 transport and storage in shale reservoirs. Applied Energy, 2023c, 331: 120444.

Wan, T., Mu, Z. The use of numerical simulation to investigate the enhanced Eagle Ford shale gas condensate well recovery using cyclic CO_2 injection method with nanopore effect. Fuel, 2018, 233: 123-132.

Xiong, W., Zhao, Y., Qin, J., et al. Phase equilibrium modeling for confined fluids in nanopores using an association equation of state. The Journal of Supercritical Fluids, 2021, 169: 105118.

Yang, Y., Song, H., Imani, G., et al. Adsorption behavior of shale oil and water in the kerogen-kaolinite pore by molecular simulations. Journal of Molecular Liquids, 2024, 393: 123549.

Yuan, L., Zhang, Y., Liu, S., et al. Investigation of the effect of CO_2 on asphaltene deposition and flow mechanism under nano-confined environment. Journal of Molecular Liquids, 2024, 396: 124092.

Zhang, K., Jia, N., Li, S., et al. Static and dynamic behavior of CO_2 enhanced oil recovery in shale reservoirs: Experimental nanofluidics and theoretical models with dual-scale nanopores. Applied Energy, 2019, 255: 113752.

Zhang, K., Jin, Z., Li, S. Coupled miscible carbon utilization-storage processes in fractured shales. Chemical Engineering Journal, 2022a, 441: 135987.

Zhang, T., Sun, S. A coupled Lattice Boltzmann approach to simulate gas flow and transport in shale reservoirs with dynamic sorption. Fuel, 2019, 246: 196-203.

Zhang, W., Feng, Q., Wang, S., et al. Pore network modeling of oil and water transport in nanoporous shale with mixed wettability. Journal of Petroleum Science and Engineering, 2022b, 209: 109884.

Zhang, Y., Yu, W., Sepehrnoori, K., et al. Investigation of nanopore confinement on fluid flow in tight reservoirs. Journal of Petroleum Science and Engineering, 2017, 150: 265-271.

Zhou, G., Duan, X., Chang, J., et al. Investigation of CH_4/CO_2 competitive adsorption-desorption mechanisms for enhanced shale gas production and carbon sequestration using nuclear magnetic resonance. Energy, 2023, 278: 127964.